Research Article | Vol. 13, No. 2 / 1 Feb 2022 / Biomedical Optics Express 571

Biomedical Optics EXPRESS

Polarization enhanced laparoscope for improved visualization of tissue structural changes associated with peritoneal cancer metastasis

ROBERT M. TROUT,[1] EINSTEIN GNANATHEEPAM,[1] AHMED GADO,[1] CHRISTOPHER REIK,[1] JESSICA C. RAMELLA-ROMAN,[2] MARTIN HUNTER,[3] THOMAS SCHNELLDORFER,[1,4,5] AND IRENE GEORGAKOUDI[1,5,*]

[1]*Department of Biomedical Engineering, Tufts University, 200 College Ave, Medford, MA 01255, USA*
[2]*Department of Biomedical Engineering, Florida International University, Miami, FL, USA*
[3]*Department of Biomedical Engineering, University of Massachusetts at Amherst, Amherst, MA, USA*
[4]*Division of Surgical Oncology, Tufts Medical Center, 800 Washington St, Boston, MA 02111, USA*
[5]*Contributed equally*
[*]*Irene.Georgakoudi@tufts.edu*

Abstract: A polarization enhanced laparoscopy (PEL) imaging system was developed to examine the feasibility of utilizing PEL to augment conventional white light laparoscopy (WLL) in the visualization of peritoneal cancer metastases. The system includes a modified tip to illuminate tissue with linearly polarized light and elements in the detection path enabling recording of corresponding images linearly co- and cross-polarized relative to the incident light. WLL and PEL images from optical tissue phantoms with features of distinct scattering cross-section confirm the enhanced sensitivity of PEL to such characteristics. Additional comparisons based on images acquired from collagen gels with different levels of fiber alignment highlight another source of PEL contrast. Finally, PEL and WLL images of ex vivo human tissue illustrate the potential of PEL to improve visualization of cancerous tissue surrounded by healthy peritoneum. Given the simplicity of the approach and its potential for seamless integration with current clinical practice, our results provide motivation for clinical translation.

1. Introduction

For patients suffering from gastrointestinal or gynecologic malignancies, selection of an effective treatment plan relies on the accurate staging of the underlying cancer. More specifically, it is vital to identify any possible distant metastases when considering the prospects of operative treatment, chemotherapy, and/or radiation [1]. Despite improvements in clinical modalities available for staging, including cross-sectional radiographic imaging (CT, MRI) and staging laparoscopy, the accuracy of staging for gastrointestinal and gynecologic malignancies remains poor in many cases [1,2]. "Under-staging" is a common problem, particularly for cancers of the pancreas, ovary, stomach, and gallbladder. Of all patients who undergo a major operative resection for malignancy under the presumed absence of distant metastasis, death from cancer progression occurs in up to 30% within 1 year after the operation [3–6]. Since these patients' metastases must have been present at the time of operation, but not detected with conventional methods, there is a critical need for improvement in technologies intended to screen for evidence of metastasis.

As the peritoneum is a common site for abdominal metastases [1], peritoneal white light laparoscopy (WLL) is considered the most effective means for detecting abdominal cancer metastasis [7]. However, significant limitations still exist in the use of WLL for peritoneal metastasis detection. Chief among these are poor sensitivity to lesions smaller than a few millimeters, and reduced specificity due to benign fibrotic changes, which appear similar to

#443926 https://doi.org/10.1364/BOE.443926
Journal © 2022 Received 21 Sep 2021; revised 17 Dec 2021; accepted 20 Dec 2021; published 5 Jan 2022

Biomedical Optics EXPRESS

malignant metastases [8]. Thus, our goal is to identify a potential imaging solution that is readily amenable to translation and integration with the current standard of care, while improving WLL diagnostic performance. Since peritoneal lesions are predominantly superficial and involve significant disruptions in the structure and organization of the extracellular stroma of "healthy" peritoneal tissue, we sought to explore the potential of polarization enhanced laparoscopy (PEL), as a relatively simple and cost-effective label-free imaging enhancement to standard WLL [9].

As neoplastic development progresses in tissue, significant changes to collagen content, collagen organization, and cellular morphology occur [10–12]. These changes result in modifications to the scattering and birefringent properties of the tissue which are detectable via optical methods including polarimetry, light-scattering spectroscopy (LSS) and second harmonic generation (SHG) imaging [13,14]. In the context of polarimetric imaging, these changes and have been found to result in a decrease in depolarization and retardance compared to healthy tissue due to reductions in scattering and birefringence, respectively [15–18]. Our motivation to implement a PEL system stems from the successful past of polarimetric imaging to exploit these changes in the realm of tissue diagnostics, from fully comprehensive spectrally-resolved state of polarization (SOP) imagers to simpler polarization-gated implementations [19–21]. The polarimetric data provided by these systems has demonstrated diagnostic potential in many varieties of cancerous tissue including breast [22–24], cervical [15,17,25–28], colon [16,29–32], oral [18], and skin [33–35]. In the case of peritoneal metastases, similar changes in cell and matrix components have been found between healthy and malignant tissue [9,36]. However, the potential of depolarization and retardance metrics detected through linearly polarized reflectance measurements to enhance detection of these metastases is currently uncharacterized.

In this study, we chose to implement RGB linear co-polarized gating for this purpose. Our reasoning behind this selection was fourfold: first, the co-polarized-gated signal increases as linear depolarization and retardance decreases [37], potentially highlighting targets like malignancies exhibiting lower depolarization and retardance than the healthy background tissue. Second, the target peritoneal metastases manifest as thin lesions at the surface of the peritoneal membrane. A major attribute of co-polarization gating includes the rejection of deeply scattered light that has likely not strongly interacted with the superficial lesion and may impede detection of superficial changes [38,39]. Third, RGB color-sensitivity can also be added to enhance visualization of features with absorbance contrast such as vasculature [40] and also enable the acquisition of regular color WLL as needed by the clinician during the procedure. Finally, while Stokes-vector, Mueller-matrix, LSS, SHG, and spectrally-resolved systems are likely to yield the most comprehensive assessments regarding tissue properties [25,41–48], the instrumentation, image acquisition and processing time required make integration into a real-time surgical guidance workflow difficult. For our application, it is necessary to make compromises for real-time video-rate image data during laparoscopic imaging to effectively guide surgical biopsy. This is not currently feasible for these systems, which have significant acquisition and processing bottlenecks regarding their maximum achievable frame rate. By contrast, faster implementations of simpler polarized systems exist, including those which are co-polarization gated [49,50]. Thus, we limited our polarimetry to linear polarization gating as a more feasible method to implement which still retains diagnostic potential.

To acquire a linear co-polarization-gated signal, co- and cross-linearly polarized reflectance are imaged under linearly polarized illumination. In this way, when a scattering tissue is illuminated, we can consider two main components contributing to the resulting total sample reflectance: light detected after undergoing multiple scattering events with deeper tissue layer components, and light scattered after one to three interactions with superficial tissue components (~1-3 mean free paths) [38]. The former scattered signal is generally randomly polarized and in principle consists of equal levels of light polarized along the parallel and perpendicular orientations, while the latter chiefly maintains its incident polarization state. The gated signal is obtained as the differential

Biomedical Optics EXPRESS

polarization signal (I_Δ), i.e. the difference between the co-polarized ($I_{|||}$) and cross-polarized ($I_\perp$) signals relative to the incident illumination:

$$I_{\parallel} - I_{\perp} = I_{\Delta} \tag{1}$$

It can be seen that this differential signal is associated with superficial reflectance from the sample as mentioned previously:

$$(I_{surface} + \frac{1}{2}I_{bulk}) - \left(\frac{1}{2}I_{bulk}\right) = I_{\Delta} \tag{2}$$

$$I_{surface} = I_{\Delta} \tag{3}$$

In this study, we present the initial evaluation of a prototype PEL system designed to image this differentially polarized signal. This is achieved via imaging of phantoms, which specifically highlight enhanced PEL sensitivity to changes in scattering cross-section and organization associated with collagen remodeling. We anticipate that sensitivity to such features may serve as a major source of diagnostic contrast to supplement WLL detection of superficial intraperitoneal metastatic lesions.

2. Materials and methods

2.1. Polarization enhanced laparoscope design

For the purposes of this study, a prototype PEL-integrated laparoscopic imaging system was designed and constructed (Fig. 1). A broadband white light source (Karl Storz Xenon 300 - 20133120) transmitted illumination across a fiber optic cable (Karl-Storz) to the distal end of the probe (Fig. 1(c)). Based on earlier reports by Woods et al. and Lindberg et al. the sapphire optical window of a standard WL Karl-Storz laparoscope with a 30 degree bevel tip (Karl Storz Hopkins II 10 mm 30-degree model 26003BA, Tuttlingen, Germany) was replaced by a fused silica window by the company to avoid the polarization effects exhibited by the sapphire window [51,52]. To polarize the illumination output from the laparoscope tip, a sheath was designed for the purpose of mounting a polarizing film in front of the output. The body of the sheath was machined from 316L stainless steel (McMaster-Carr) with an outer diameter of 11.6 mm such that it can be easily inserted through a standard 12 mm trocar employed during laparoscopy procedures. The tip of the sheath consisted of a cap of the same material beveled at the same angle as the laparoscope, with a 1.73 mm thick amorphous glass window seated inside, adhered with medical-grade epoxy (EPO-TEK 301, Epoxy Technology). A reflective linear polarizer (XP40HT, Edmund Optics) cut in the shape of the illumination output (crescent) was affixed onto the window using the self-adhesive to polarize the illumination (Fig. 1(d)).

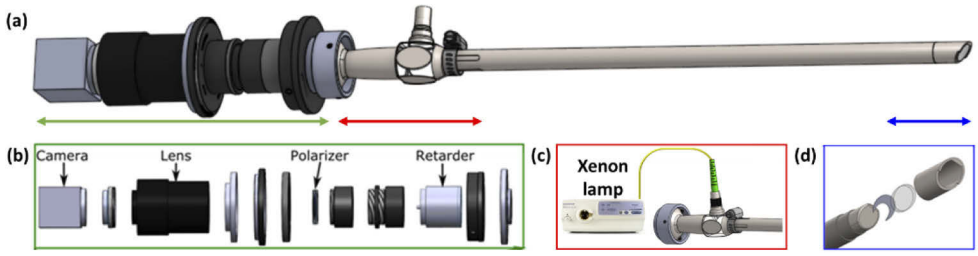

Fig. 1. (a) Assembled PEL laparoscopic probe. Detailed (b) proximal optical assembly, (c) adapters, and (d) distal cap with polarizing film and amorphous glass window. Colored arrows under panel (a) schematic are shown in more details in panels b-d.

Biomedical Optics EXPRESS

Reflectance from the sample was collected and relayed through a tunable waveplate with slow axis oriented 45 degrees with respect to polarization direction of the illumination. After passing through a linear polarizer oriented parallel to the illumination, the image was captured by an RGB CCD camera (FLIR Blackfly 23S2C-CS) (Fig. 1(b)). The variable waveplate was an electrically controlled liquid crystal (Thorlabs LCC1111T-A) whose degree of retardance can be varied through the application of different voltages by its controller. Two voltages were used during operation, switching between 25 V (zero retardance) and 1.6 V (half-wave retardance) after each frame was integrated by the camera. In this way, the co- and cross-polarized components of the image relative to the illumination polarization were incident on the polarizer at 0 or 90 degrees depending on the rotation imposed by the retarder voltage (Fig. 1(b)). Switching off the retarder state resulted in switching which polarized image, co- or cross-, was passed by the polarizer and imaged by the camera. This switching was synchronized with frame collection utilizing the camera's built-in strobe feature. This allowed the camera to output a trigger following the completion of a frame's exposure, directing the switching of the retarder voltage for the exposure of the next frame. As the camera captured at 27 frames per second the waveplate switched 27 times per second. There was a 10.2 ms dead time between each frame to accommodate complete switching of waveplate. The camera recorded 12-bit depth RGB images of size 1920 by 1200 pixels, captured at 27 frames per second, with an angular field of view of 34 degrees and resolution of 50–100 μm at the working distance of 5 cm (estimated by imaging a 1951-USAF resolution target using both WLL and PEL). The series of collected images alternating in polarization state were then processed in real-time on an external computer using a custom Python software program. A new stream of images was generated from the alternating co- and cross-polarized image data, with PEL images computed as the difference of each pair of raw polarized images, and the corresponding unpolarized WLL images computed as their sum. To assess the sensitivity of the PEL system to the detection of linearly co-polarized reflected signals we acquired measurements from a polarization-maintaining silver mirror. Less than 9% of incident linearly polarized light was depolarized by various optical components of the polarization enhanced laparoscope.

2.2. Polydimethylsiloxane (PDMS) optical phantom design and characterization

To assess the sensitivity of the PEL system to changes in scattering cross-section, a PDMS-based mold with a range of size features was constructed. The casting mold for the features of the phantoms was printed on a mold on a Form 2 3D printer (Formlabs) from dental resin (Formlabs). The features printed consisted of an array of square pillars with varying height and width to create a series of model nodules of sizes varying in height from 0.1 to 1 mm and length and width from 0.05 to 1 mm. The resulting printed mold was placed at the bottom of a plastic 35 mm petri dish (Fig. 2(a)) and cast with a mixture of PDMS (10:1 base: curing agent by mass) and 0.052% weight by mass TiO_2 powder (Titanium dioxide powder, Rutile, particle size 0.3–1 μm, Atlantic equipment engineers) (Fig. 2(b)). After degassing the mixture for 1 hour to remove air bubbles, the phantom was cured at 60 °C for 1 hour. The cast was removed and trimmed (Fig. 2(c)), and the feature PDMS mixture, containing 1.058% ZnO (Zinc Oxide particles, particle size: 0.108–0.132 μm, Essential Depot Inc), was cast against it (Fig. 2(d)). The PDMS mixtures constituting the feature and background material were prepared by first mixing the optical agent (TiO_2 or ZnO powder) with the curing agent and sonicating for 20 minutes to mix. The result was degassed, compressed face down in a glass-bottom petri dish, and cured by baking in 60° C oven for one hour (Fig. 2(e)), yielding the final phantom (Fig. 2(f)).

To confirm the presence of distinct scattering properties within the feature and background region of the phantoms, diffuse reflectance measurements were performed from separate ZnO and TiO_2 PDMS phantoms constructed with similar concentrations (SkinSkan spectrofluorometer, Horiba Jobin Yvon). The diffuse reflectance measurements were repeated three times and

Biomedical Optics EXPRESS

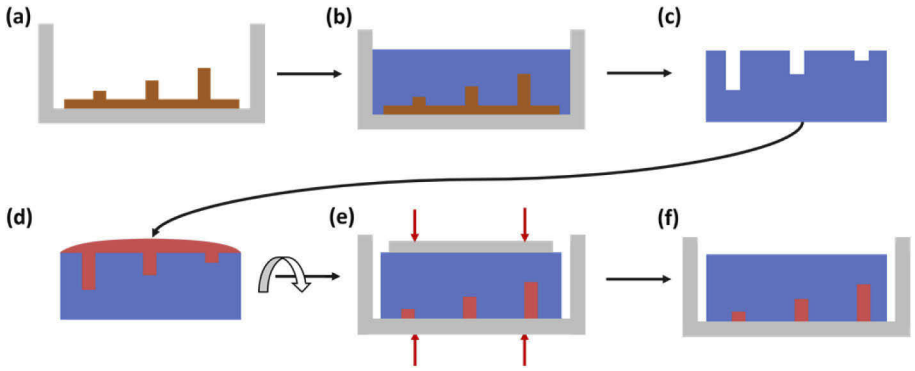

Fig. 2. Fabrication method for PDMS optical tissue phantoms (a) 3D-printed mold containing the phantom features is seated in a small petri dish. (b) The dish is filled with PDMS with the background optical agent mixed in. (c) The PDMS is removed from the mold and inverted. (d) PDMS with the feature optical agent mixed in is poured in the feature cavities. (e) The phantom is compressed against the glass bottom of the petri dish to remove excess feature PDMS, (f) Resulting optical tissue phantom mimicking a series of features of varying width and thickness with a distinct scattering profile from that of the background, to be imaged through the glass bottom of the dish.

the reduced scattering coefficients of ZnO and TiO_2 were computed from diffuse reflectance measurements using an in-house inverse Monte Carlo program built on the Matlab platform [53]. To understand the difference in scattering cross section of background and feature, the extracted scattering coefficients were fitted to the generic formula, $\mu_s' = a\ \lambda^{-b}$ [54]. The parameters a and b depend on the concentration of scatterers and scattering cross section, respectively. Further, to quantify the feature visibility of the PDMS phantom in WLL and PEL modalities, an intensity profile along different features and background was computed. Subsequently, the signal to background ratio (SBR) was estimated using the ratio of the mean intensity within the features and the background. To compute the SBR for features of different dimensions different areas of 20×20, 7×7, 5×5, 3×3, or 1×1 pixels at the center of the features were considered for signal and a corresponding area at the periphery of the feature was considered for background.

2.3. Collagen gel phantoms

Collagen gels were fabricated from rat tail collagen Type I solution (Corning) to test the sensitivity of the instrument to tissue birefringence. A collagen concentration of 2.9 mg/mL in 0.02 N acetic acid was made, and 0.8 mL of the gel solution was added onto a 35 mm glass bottom dish and incubated at 37 °C for 45 minutes. Following a previously described method to enhance the alignment of the collagen fibers in these gels, we built micro-rakes that were inserted in the gels at a separation distance of 2 mm. Each cylindrical rake protrusion was 1 mm in diameter and 10 mm in height and was constructed from dental resin using a Form 2 3D printer (Fig. 3) [55–57]. The rakes were pulled apart from each other using a 2-dimensional translation stage controlled (Newport 855C Programmable Controller) to move at a speed of 3 µm/s until a strain of 15% was applied on the collagen gel phantom. Measurements were acquired from eight collagen gels. Such gels were also used along with excised tissue to evaluate the dependence of PEL to variations in the orientation of collagen fibers relative to the axis of the linearly polarized illumination. This was done by rotating the sample from 0° to 360° with a step size of 10° and acquiring co-polarized and cross-polarized images using PEL.

To validate that the stretching of the gels resulted in increased fiber alignment, gels were imaged using 3D confocal reflectance microscopy while they were being stretched, using a Leica

Biomedical Optics EXPRESS

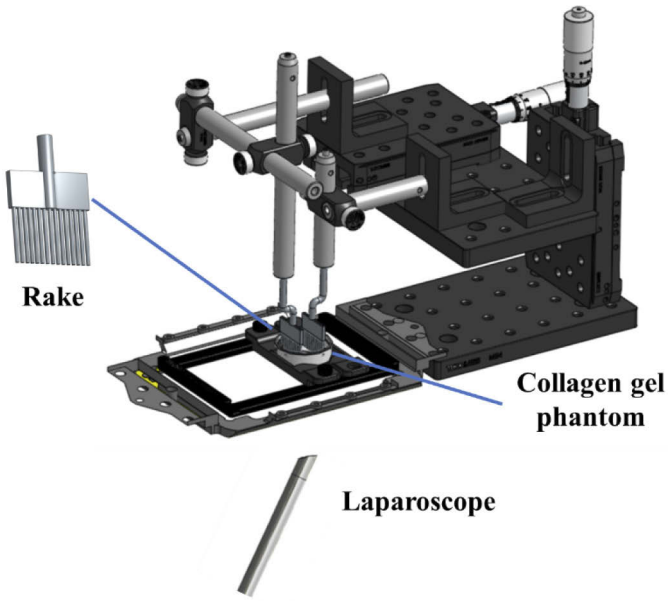

Fig. 3. Micro strain device setup used for stretching of collagen gel. Each cylindrical rake protrusion was 1 mm in diameter, separated by a distance of 1 mm and 10 mm in height.

SP8 confocal microscope and moving the microscope brightfield illumination arm so that the stretching apparatus could be placed on the stage. A 25x (1.1. NA) water-immersion objective was used to acquire 455 × 455 µm images, over a depth of 50 µm in 1 µm steps. The 3D orientation of the collagen fibers was assessed using a previously described algorithm [56–59]. The algorithm involves selection of fiber-only regions using Otsu thresholding and characterization of the 3D orientation of fibers using a weighted vector sum approach that provides the polar and azimuthal angles of fiber orientation in a 3D specimen. The distribution in the values of these angles is used to determine the 3D directional variance as a quantitative metric of fiber alignment that varies between 0 and 1 for perfectly aligned and randomized fibers, respectively. The algorithm for these assessments is available at https://engineering.tufts.edu/bme/georgakoudi/publications -Liu et al. Biomaterials 2016.

2.4. Animal tissue preparation

Flexor digitorum longus (FDL) tendons were a kind donation from Brianne Connizzo at Boston University. They were harvested from healthy, young mice, following CO_2 euthanasia and stored at 4°C in phosphate buffer saline (PBS). The thickness of the FDL tendons were 200–300 µm and 15–18 mm in length. Imaging was performed within three days using PEL. Rat oral mucosal and submucosal tissues were excised following CO_2 euthanasia, snap frozen in liquid nitrogen, and kept at -80°C. Prior to PEL and SHG imaging, the samples were thawed and stretched to ensure a smooth surface. In both cases, the tissues were excised following euthanasia from rodents participating in unrelated Institutional Animal Care and Use Committee approved protocols and were considered discarded tissues.

2.5. Fixed human tissue specimens

Hematoxylin and eosin-stained histology slides of six lesions were obtained from patients who underwent laparoscopic surgery at Lahey hospital, Burlington, MA. Three of the lesions were histologically confirmed to be malignant, whereas remaining 3 were benign. The biopsy samples

Biomedical Optics EXPRESS

had 8–10 µm thickness. Confocal image acquisitions were made from 2 region of interests (ROI) from each lesion. The biopsy slides were obtained with informed consent of the patient and Institutional Review Board clearance from the hospital.

2.6. Ex vivo human specimen

To model a metastatic peritoneal lesion, a biopsy specimen of healthy peritoneum and from a primary ovarian cancer was collected from a single patient who underwent operative resection for an ovarian cancer. In this case, there was no indication of metastases on the peritoneum. Ovarian cancers, which often metastasize to the peritoneum, are characterized by low collagen area fraction and directional variance with respect to healthy ovarian and peritoneal tissues [9,60–62]. Since the size of the peritoneal metastases can range from 0.4 to 31.7 mm^2, a "peritoneal metastatic model" was simulated by placing a ~1mm^2 excised portion of the primary tumor atop the healthy peritoneum biopsy. This model was then imaged in WLL and PEL modalities. Studies were approved by the Lahey Clinic Inc. Institutional Review Board.

2.7. Image analysis

The recorded PEL images were post processed to reduce detector noise and assess color based PEL contrast. Each RGB image was converted to Lab space where image L contains luminosity and images a and b contain information regarding their color. Gaussian smoothing (2-D Gaussian smoothing kernel with standard deviation of 0.5) and contrast adjustment were applied on L, while images a and b were unmodified. The processed image was converted back to RGB space for analysis.

A quantitative comparison of feature visibility was conducted for corresponding PEL and WLL based on Weber contrast. Weber contrast (C_w) is a function of feature intensity (I_f) and background intensity (I_b), and defined as [63]

$$C_W = \frac{I_f - I_b}{I_b} \tag{4}$$

In each computation, I_f and I_b were approximated as the average intensity of the nodule and the surrounding background, as defined by manually defined ROIs. A buffer region of area equal to that of the ROI, defined by expansion of the ROI border, where there is a transition of malignant lesion into background tissue was not considered for analysis. The subsequent portion of healthy peritoneal tissue of area twice that of the lesion ROI was considered as the background region.

2.8. Polarization-sensitive Monte Carlo simulation

We applied the Monte Carlo program written in C language developed by Ramella-Roman et al. to simulate polarized light propagation in a medium composed of spherical particles [64]. The program launched 10^8 photons, then tracked and recorded the Stokes vector of photons after every reflection, refraction, and scattering event until all the photons were absorbed or escaped from the medium. The alteration of the Stokes vector due to reflection and refraction at the sample/environment interface was computed using Fresnel's and Snell's equation, respectively. The Mie function was used to describe scattering properties of the medium. The index of refraction of the sample medium was assumed to be 1.4, and the surrounding environment was assigned an index of refraction of 1. A series of 12 simulations were performed to compute the intensity of WLL and PEL in the units of fraction of incident photon by varying the scattering cross section of the particles in the range of 0 to 2 μm^2 at 500 nm. The concentration of the particles was altered such that the reduced scattering coefficient remained at a constant value of 10 and 20 cm^{-1}.

Biomedical Optics EXPRESS

2.9. Statistics

The collagen gel phantom image analysis outcomes were subjected to statistical analysis. The mean and standard deviation values of all the variables were calculated and a two-tailed t test was performed to determine the level of significance (P value). Significance level for all statistics was set to $\alpha = 0.05$. All statistical analyses were performed in IBM SPSS statistics 26.

3. Results

3.1. PDMS tissue phantom with altered scattering cross section

The experimental setup to acquire WLL and PEL images from the phantom is shown in Fig. 4(a), imaging at a working distance of 5 cm and at 30° angle relative to the surface of the phantom to reduce glare. The tissue phantoms (Fig. 4(b)) comprise an array of twenty-one different feature geometries. Each row contains features of the same area with decreasing height from left to right ranging from 1 mm to 0.1 mm. Each column contains features of the same height, while the area dimensions are varied ranging from 1×1 mm to 50×50 μm^2. This range of feature sizes was considered as a means to assess the sensitivity limitations of PEL with respect to feature sizes. A confocal reflectance microscopy image from the surface of the $100 \times 100 \times 100$ μm^3 phantom feature illustrates that the actual dimensions of even the smaller features were close to specifications, even though the shape deviated from the designed square (Fig. 4(g). The enhanced reflectance intensity of the feature is suggestive of distinct scattering properties. This is confirmed by diffuse reflectance spectroscopic measurements performed to assess the reduced scattering coefficients from the background and features (Fig. 4(h). From these spectra, the reduced scattering coefficients at 500 nm of the background and feature appear similar. However, the wavelength dependence of the diffuse reflectance spectra and corresponding reduced scattering coefficient (μ_s') follows very different trends, indicating that they correspond to features with different scattering cross sections. Representative μ_s' spectra and corresponding fits acquired using the expression $\mu_s' = a\,\lambda^{-b}$ yield b values of 1.774 and 0.098 for ZnO and TiO_2 features, respectively. As both ZnO and TiO_2 particles are submicron, the difference in the scattering cross section is primarily attributed to differences in the refractive index of these particles.

Figures 4(c), e include representative images of the phantoms acquired in WLL and PEL imaging modalities respectively, highlighting enhanced contrast in the PEL image for features that appear very faint in WLL. The image 4e looks black and white because the depolarization is similar for different color bands and this may be due to the fact that the PDMS phantom consists of only scatterers and no absorbers. To quantify the differences in contrast, the intensity profiles of WLL and PEL images are examined (Fig. 4(d) and (f)), while Table 1 and 2 list the signal to background ratio for all the features in WLL and PEL imaging (n = 3). It is evident that PEL imaging provides an improvement in the visualization of features of all dimensions compared to WLL (Table 1 and 2). The signal to background ratio for PEL is 1.5 to 2 times higher than WLL for features of different dimensions.

Table 1. Signal to background ratio for features of different depth and size in WLL imaging of PDMS phantom

Depth → Size ↓	1 mm	0.5 mm	0.25 mm	0.2 mm	0.15 mm	0.1 mm
1 mm	1.32 ± 0.06	1.12 ± 0.05	1.08 ± 0.06	1.06 ± 0.05	1.05 ± 0.05	1.04 ± 0.05
0.5 mm	1.21 ± 0.04	1.09 ± 0.04	1.05 ± 0.03	1.03 ± 0.04	1.02 ± 0.04	1.01 ± 0.04
0.25 mm		1.07 ± 0.04	1.04 ± 0.04	1.03 ± 0.04	1.03 ± 0.03	1.03 ± 0.03
0.1 mm				1.03 ± 0.02	1.03 ± 0.03	1.03 ± 0.02
50 μm						1.00 ± 0.01

Biomedical Optics EXPRESS

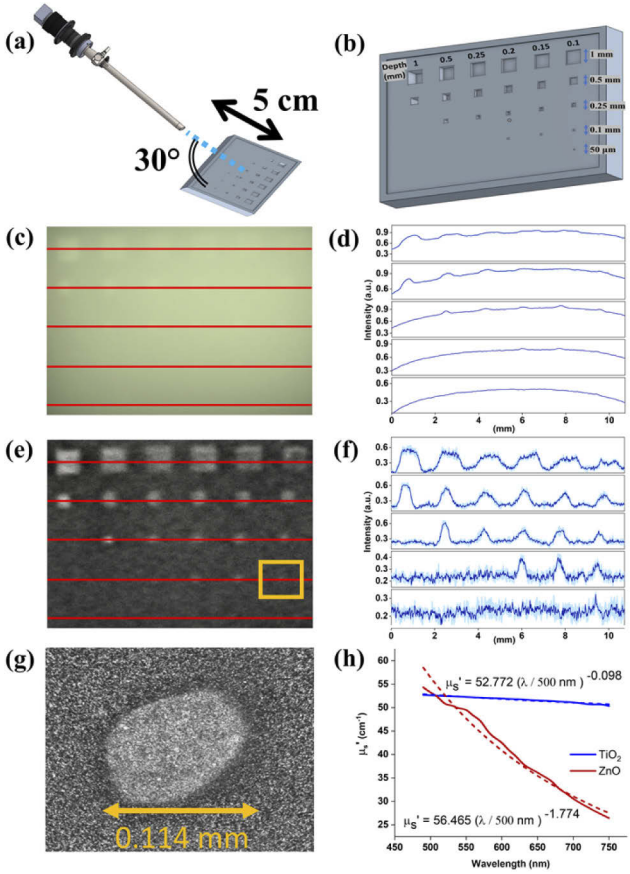

Fig. 4. (a) Image acquisition setup for WLL and PEL. (b) PDMS tissue phantom with TiO_2 as background and ZnO as feature with varied size and depth. Imaging of tissue phantom in (c) WLL and (e) PEL modalities and (d and f) their corresponding intensity profile (along red lines of (c) and (e)) with standard deviation from three different acquired images indicated as a blue shade, not visible for the WLL profiles because it is very small. (g) Confocal microscope image of the phantom feature indicated by yellow square in panel f, expected to be $100 \times 100 \times 100$ µm. (h) Reduced scattering coefficient measurements of background and feature computed from diffuse reflectance measurements.

Table 2. Signal to background ratio for features of different depth and size in PEL imaging of PDMS phantom

Depth → Size ↓	1 mm	0.5 mm	0.25 mm	0.2 mm	0.15 mm	0.1 mm
1 mm	3.36 ± 0.14	2.95 ± 0.02	2.69 ± 0.03	2.54 ± 0.04	2.26 ± 0.03	2.05 ± 0.01
0.5 mm	3.11 ± 0.15	2.31 ± 0.08	2.28 ± 0.10	2.21 ± 0.03	2.06 ± 0.12	2.01 ± 0.08
0.25 mm		2.26 ± 0.04	2.20 ± 0.03	1.90 ± 0.06	1.82 ± 0.13	1.69 ± 0.01
0.1 mm				1.65 ± 0.08	1.61 ± 0.08	1.50 ± 0.09
50 µm						1.25 ± 0.03

To better understand the mechanism of this improvement, the scattering cross sections of the phantom background and feature were computed based on Mie theory using the size and

Biomedical Optics EXPRESS

refractive index of TiO2 and ZnO particles. Then, the dependence of WLL and PEL intensity on scattering cross section was simulated using Monte Carlo simulations that take into account the polarization of the incident light (Fig. 5) [64]. The concentration of the scatterers of different size were varied such that the scattering coefficient remained constant. According to Mie theory, the scattering cross section of the TiO2 and ZnO are 0.951 μm^2 and 0.00216 μm^2 respectively at 500 nm [65]. Based on previous studies, it is known that the mechanism behind this difference in contrast originates with the differences in the scattering cross section of the background and feature optical agents [66,67]. The simulation results corroborate the enhanced dependence of PEL measurements to different scattering cross-sections, with the PEL intensity increasing with smaller scattering cross section, while WLL intensity remaining largely the same. Further, it is observed from Fig. 5, that the PEL signal is less dependent on changes in scattering coefficient. This is attributed to the fact that the change in the stokes vector of the incident light is primarily determined by the size of the scatterer, which affects its scattering cross section. An increase in scattering coefficient may reduce the depth selectivity of PEL signal, but the extent of depolarization is unaffected by the altered scattering coefficient [38]. In this way, the difference in scattering cross section of the two media serves as a source of PEL contrast not available to WLL; the higher cross section in the background reduces the PEL intensity compared to the features possessing a lower cross section, manifesting the features on a darker background.

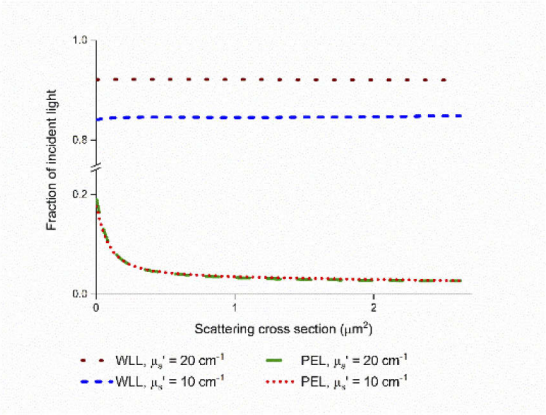

Fig. 5. Monte Carlo simulation of WLL and PEL intensity for scatterers of different scattering cross section where the concentration of scatterers varied such that WLL remains constant.

3.2. Collagen gel-based tissue phantoms with altered birefringence

Earlier studies have established that changes in collagen fiber alignment will influence the polarization state of scattered light [68,69]. To assess the sensitivity of PEL images to the organization of collagen fibers, which are typically the predominant scatterers in a tissue such as the peritoneum, we acquired PEL images of collagen hydrogels whose fiber orientation was modified by stretching the gel perpendicular to the direction of polarization of incident light using the apparatus shown in Fig. 3. Representative confocal images acquired before and following stretching are shown in Fig. 6(a and b) color coded according to the 3D directional variance of each pixel (3D directional variance is a number that varies between 0 and 1, corresponding respectively to completely aligned and randomly oriented fibers) [56]. Figure 6(c) shows the population of fibers along different polar angles for a representative unstretched and stretched collagen gel. The 3D variance of fiber organization within 8 collagen gels is found to decrease

Biomedical Optics EXPRESS

when the collagen gel phantoms are stretched indicating that the fibers align in the direction of applied strain (Fig. 6(d)).

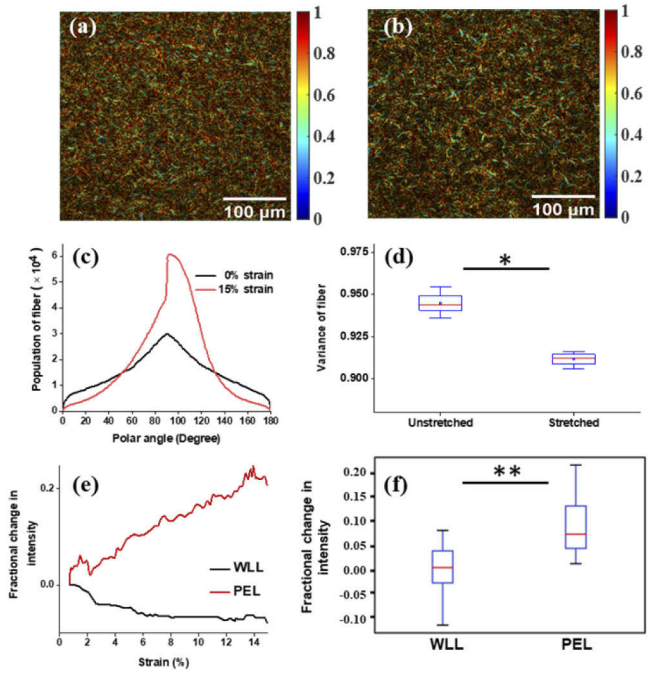

Fig. 6. 3D variance-pseudocolored confocal images of collagen fibers of (a) unstretched and (b) stretched collagen gel. (c) Population of fibers with respect to different polar angles. (d) 3D variance of collagen fiber organization of 5 collagen gel phantoms in unstretched and stretched positions. (e) Mean intensity of WLL and PEL images with respect to time when the collagen is stretched and (f) percentage change in intensity for WLL and PEL imaging when the collagen gel is stretched. *denotes p-value $< 10^{-5}$, n = 8 and **denotes p-value < 0.05, n = 8

A total of eight collagen gels were imaged in WLL and PEL during stretching, with changes in the signal intensity recorded over the course of the stretch for each modality (representative recording from one gel is shown in Fig. 6(e)). From these series, a fraction change in the initial intensity value over the course of the experiment was computed (Fig. 6(f)). As expected, in WLL imaging, there is no significant difference between the unaligned and stretched collagen gels, whereas in PEL, the fraction change values are significantly higher in the stretched than in the initial state (p-value = 0.031). These results also highlight enhanced sensitivity of PEL relative to WLL imaging to fiber alignment.

Finally, we sought to characterize the impact of the anisotropy characteristics of tissue on PEL intensity. We acquired PEL images from unstretched and stretched collagen gels as well as from excised mouse tendon and rat mucosal tissue. Representative 3D variance pseudocolored SHG images from tendon and mucosal tissues (Fig. 7(a, b)) along with corresponding images from collagen gel samples (Fig. 6(a, b)) highlight the wide range of collagen organizations they represent. It is observed that the normalized standard deviation of the PEL intensity for different orientations (0°-360° sampled with a step of 10°) of the samples are 0.49 ± 0.03, 0.11 ± 0.02, 0.09 ± 0.03, 0.06 ± 0.02 for mouse FDL tendon, rat oral mucosa, stretched and unstretched collagen gels, respectively (Fig. 7(d)). As expected, the orientation of the preferred alignment of the collagen fibers relative to the polarization axis affects the PEL but not the WLL signal levels

Biomedical Optics EXPRESS

(Fig. 7(d-f)). However, the size of this effect depends on the level of collagen fiber alignment. The dependence observed for the tendon sample is an extreme tissue case, where all collagen fibers are aligned at a level far higher than the collagen fiber organization we are likely to encounter in the peritoneum. In fact, assessment of 3D variance of collagen fibers of histological fixed tissue sections from benign and malignant peritoneal tissues yielded values of 0.89 ± 0.09 and 0.74 ± 0.12, respectively. These are values closer to those of the stretched collagen fibers (Fig. 6(d)) and the rat oral mucosa (Fig. 7(c)). For these two types of samples the normalized standard deviation of the PEL signal intensity is 0.09 ± 0.03 (stretched collagen fiber samples) and 0.11 ± 0.02 (oral mucosa), indicating variations on the order of 10%.

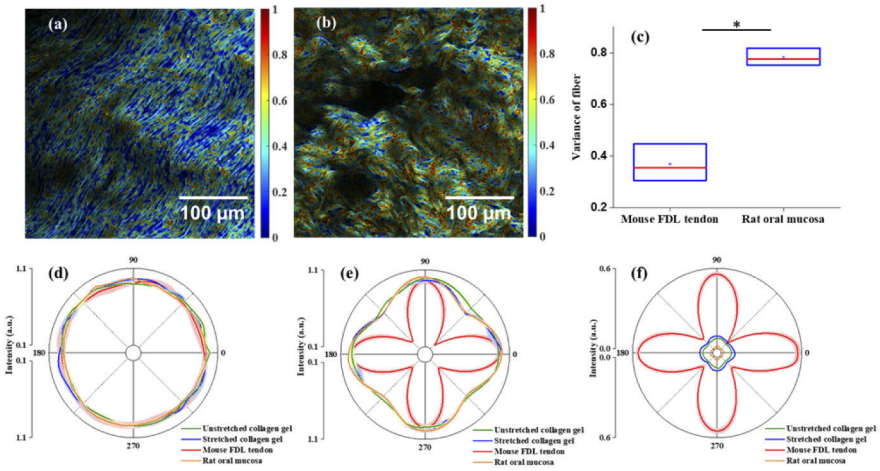

Fig. 7. 3D variance-pseudocolored images of collagen fibers of (a) mouse FDL tendon and (b) rat oral mucosa. (c) 3D variance of collagen fiber organization of 3 ROIs of mouse FDL tendon and rat oral mucosa. (d) Normalized WLL, (e) normalized PEL, and (f) PEL intensity at different orientations of samples relative to the illumination polarization angle for unstretched and stretched collagen gels, mouse FDL tendon and rat oral mucosa with their corresponding standard deviation for three different measurements indicated as a shaded region. *denotes p-value $< 10^{-3}$, n = 3.

3.3. *Ovarian tumor biopsy placed on healthy peritoneal tissue*

To illustrate the potential of PEL to enhance visualization of small superficial peritoneal metastatic lesions, we acquired images from a freshly excised healthy peritoneum specimen, on top of which we placed a small (1 mm^3) ovarian tumor tissue specimen. The RGB images are shown along with the individual color channel images for WLL and PEL imaging (Fig. 8(a-d) for WLL, (e-h) for PEL).

When transitioning from WLL (Fig. 8(a)-(d)) to PEL (Fig. 8(e)-(h)) imaging, it is immediately apparent that there is improvement in the visibility of the model lesion in all color channels. The improvement appears most prominently in the red channel, while it is subtler in the green and blue channels. This is confirmed quantitatively through Weber contrast measurements for WLL and PEL images based on the feature and background ROIs indicated in the Figure (Fig. 8(i)).

Biomedical Optics EXPRESS

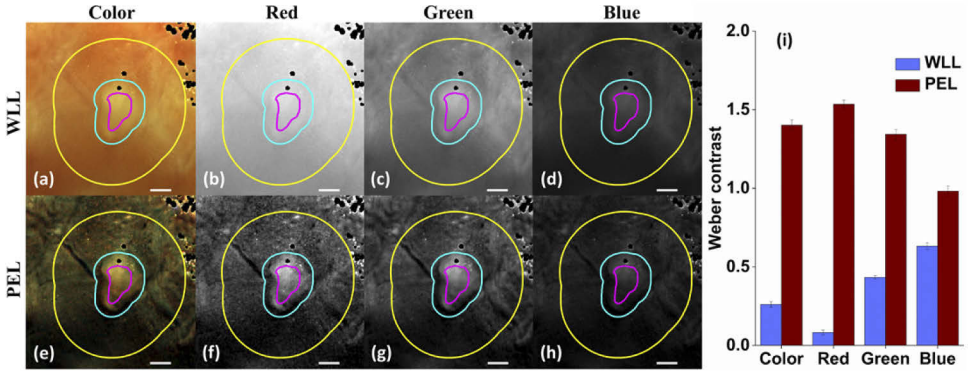

Fig. 8. Imaging of a human ovarian tumor biopsy (circled in magenta) placed atop a human peritoneum biopsy. 7a was taken in conventional non-polarized RGB, while 6e was imaged in PEL mode. The corresponding individual red, green, and blue channels are displayed alongside each image. 1 mm scale. (i) Computation of Weber contrast for quantification of nodule visibility. To estimate the Weber contrast the region enclosed by the magenta contour is considered as the lesion and the region between the cyan and yellow contours is considered as the background. The error bars indicate standard deviation of intensity for different points in the ROI.

4. Discussion

We present the design of a simple PEL system along with preliminary in vitro and ex vivo measurements highlighting the potential of this imaging system to exploit sources of contrast in peritoneal metastases not available or as pronounced in WLL. Such sources of contrast include the scattering cross section and organization of collagen fibers, which are the most prevalent components of peritoneal tissue, residing immediately below a thin peritoneal epithelium. Previous polarimetric imaging studies demonstrated that healthy tissue is more depolarizing than cancerous tissues [18,32,34,48,17]. This implies that healthy tissue would be attenuated in PEL imaging compared to malignancies, increasing PEL contrast, consistent with our premise and findings. Data from our prior studies consisting of high-resolution, two photon microscopic imaging of malignant tissues including peritoneal metastases indicate that such tissues contain a lower collagen volume fraction and fibers with reduced diameter compared to healthy tissues, corresponding to an expected reduced scattering cross section of the malignant tissue [9]. Other studies regarding different tissues have reported similar collagen organization changes between healthy and malignant tissues [56,70–72], which have been found to lead to changes in the birefringent nature of tissue [9,67]. These alterations are consistent with the reduced randomization and depolarization of backscattered light, increasing PEL signal within lesions [67].

To validate the enhanced sensitivity of the PEL instrument to changes in scattering cross-section and collagen fiber organization, we performed measurements using PDMS-based phantoms and collagen gels. The ZnO-containing features of the phantoms model the low scattering cross section of the smaller collagen fibers expected within peritoneal malignancies, while the TiO_2-containing background models the comparatively higher scattering cross section of healthy peritoneum fibers. As anticipated, PEL imaging demonstrated improved contrast and visibility of features compared to WLL for a range of sizes and thicknesses as small as 100 µm, which were not visible via WLL (Fig. 4, Tables 1 and 2). Based on previous studies, we expect that the mechanism behind this difference in contrast originates with the differences in the scattering cross section of the background and feature optical agents [66,67]. However, we also noticed that

Biomedical Optics EXPRESS

the PEL signal to background ratio increased with feature depth up to 1 mm and cross-sectional area of the feature. This is somewhat unexpected, given that the depth selectivity of PEL was thought to be less than the maximum feature depth of 1 mm for this feature medium. We believe that the most likely origin of this effect is the settling of the scattering particles that occurs during curing. It is possible that because the features were cured face-down (Fig. 2(e)), there was some settling of the ZnO scattering agent due to gravity. This would result in a greater accumulation of scattering agent at the surface of the thicker features, potentially increasing the PEL signal due to the packing of the scatterers at the feature surface. Additionally, surface roughness could also possibly contribute to these changes [73], however we anticipate the surface of the phantoms to be smooth. there to be variance in the among the different substantial enough to result in a bias in the detected PEL signal. Prior work has demonstrated that a difference in RMS roughness on the order of a factor of two is necessary to result in just a 2% shift in the degree of linear polarization [73]. Under our fabrication method, this degree of roughness variation would be unlikely, let alone at variations that would cause more substantial depolarization.

PEL measurements were also sensitive to changes in collagen fiber orientation, while this was not the case for WLL measurements (Fig. 6). When aligned parallel with the illumination polarization axis upon stretching, the birefringent collagen fibers impart less rotation to the incident illumination [74]. This results in a greater fraction of co-polarized backscattered light compared to the randomly oriented fibers of the unstretched state. Consequently, the PEL signal intensity increases due to the greater fraction of co-polarized reflectance. The slight decrease in WLL signal observed over the course of stretching is attributed to the thinning of the sample.

However, the level of this enhancement is dependent on the preferred orientation of the collagen fibers relative to the incident polarization axis. For the application of PEL to the detection of peritoneal metastasis, we do not expect this to be a major limitation, because the collagen fibers in these tissues, even the metastatic lesions, exhibit high level of directional variance (0.89 ± 0.09 vs 0.74 ± 0.12 for healthy and metastatic lesions). Circularly polarized light would not exhibit this anisotropy dependence [74]; however, circularly polarized light was not considered in our study since the rate of depolarization with depth of circularly polarized light is slower than that of linearly polarized [75]. As mentioned previously, peritoneal metastases are superficial, and the use of linearly polarized light is expected to enhance suppression of the signals emanating from the deeper tissue layers which do not exhibit the collagen remodeling features characteristic of cancers.

To highlight the potential relevance of PEL imaging for human studies, we present an example of WLL and PEL images acquired from a 1 mm^2 freshly excised human ovarian cancer tissue biopsy placed on top of healthy human peritoneum (Fig. 8). Earlier studies reported that metastatic cancer tissues retain most genomic features of the primary tumor at the biological level, while desmoplastic reactions and extra-cellular collagen deposits are not significantly different between primary tumors and metastases [76,77]. In this way, our metastatic tissue model is a limited, yet reasonable representation of the lesions we are likely to encounter in vivo. The full color image, as well the images acquired within the red, green, and blue channels of the camera, all indicate enhanced PEL contrast within the cancerous lesion. Interestingly, the contrast provided by PEL appears to increase with wavelength, while that of WLL decreases. It is likely that these differences have their origins in the differential weight of scattering and absorption as a source of contrast for the two modalities. It will be interesting to assess the consistent presence of such wavelength differences in vivo and examine the impact of absorption as a differential source of contrast.

We note that in the context of skin, cross-polarized imaging with single or dual-wavelength illumination has been shown as a highly promising modality to detect changes in collagen architecture [40,78–81]. As the skin stromal layer is typically found a few hundred microns deeper from the surface, detection of cross-polarized scattering light would be more sensitive to

Biomedical Optics EXPRESS

such changes. In the case of the peritoneum, the epithelium consists of single thin layer of cells and metastatic lesions are in most, but not all, cases very superficial. For this reason, we exploit differential polarization in our PEL system.

The phantoms designed in our study demonstrate the increased depolarization of backscattered light from scattering features of low scattering cross section and/or low birefringence and varying size. The methodology developed for the generation of features of a small, controlled geometry proved to be quite successful in our case, and is worth noting for the benefit of other studies: the increased availability of high-resolution 3D printing allows the simple and versatile fabrication of precise phantom geometry which can be faithfully replicated in a PDMS casting containing the researcher's optical agents of choice. In the future there are many other potential phantom permutations to investigate based on their prior success [82]. Specifically, we believe that the use of glass fibers as birefringent agents in the phantoms could be very interesting: at the expense of biological accuracy provided by collagen fibers, glass fibers can be implemented in PDMS phantoms in a more controlled fashion with greater shelf life. It has been demonstrated that the degree of birefringence exhibited by the fibers can be modulated via strain [83]; in the case where it is embedded in PDMS, the phantom possesses some flexibility and can be elastically strained and relaxed to influence birefringence consistently. The greater degree of control provided by such phantoms would improve the ability to draw connection between observed phenomena and their mechanisms. That is not to say biologically faithful phantoms have no place, quite the contrary, they are frequently used successfully in the form of animal models, cell cultures, and tissue biopsies, and we have used such models in this study as well [82–89]. However, the prior knowledge afforded by synthetic phantoms can greatly aid the investigation of tissues like peritoneal metastases whose characteristics, variety, and context are complex and the topic of ongoing research.

Finally, it is important to highlight that WLL imaging can be performed simultaneously with PEL imaging, since the former simply involves addition of the co- and cross-polarized imaging. This is advantageous since the surgeon would still have access to the WLL images that they routinely use, along with the PEL images that may highlight lesions with distinct scattering properties. In this way, the enhanced sensitivity of PEL to scattering cross-section and organizational changes as opposed to overall scattering levels may also be an important means via which PEL imaging may augment WLL to improve identification of malignant lesions.

5. Conclusion and future directions

This study describes the successful design and fabrication of a polarization-enhanced laparoscope for use in staging laparoscopy. Our initial studies highlight the potential of this simple design to provide enhanced contrast for features characterized by distinct cross-sections or organization of scattering centers. Such differences have already been identified by previous high-resolution microscopic imaging studies of peritoneal tissues and motivate the translation and testing of PEL in the clinic. The ease with which WLL and PEL can be integrated from an instrumentation and implementation perspective and the potential for complementary dependence on the nature of absorption and scattering contrast further support their combined use to improve detection of peritoneal metastases during staging laparoscopy.

Funding. National Science Foundation (I531683); Office of Research Infrastructure Programs, National Institutes of Health (S10 OD021624); National Institutes of Health (R21EB23498).

Acknowledgements. The authors would like to thank Prof. Mark Cronin-Golomb, for technical support, Dr. Brianne K Connizzo for the tendon tissue donation, and Dr. Michael Esmail for assistance with rodent tissue procurement.

Disclosures. RT, MH, TS, and IG are co-authors of a submitted patent related to the polarization enhanced instrument described in this study.

Data Availability. Data underlying the results presented in this paper are not publicly available at this time but may be obtained from the authors upon reasonable request.

Biomedical Optics EXPRESS

References

1. C. M. J. Townsend and D. R. Beauchamp, "Sabiston Textbook of Surgery: The Biological Basis of Modern Surgical Practice, 19th Edition," (2012).
2. H. Yoon and D. H. Lee, "New approaches to gastric cancer staging: Beyond endoscopic ultrasound, computed tomography and positron emission tomography," in *World Journal of Gastroenterology*, (2014).
3. W. R. Jarnagin, L. Ruo, S. A. Little, D. Klimstra, M. D'Angelica, R. P. DeMatteo, R. Wagman, L. H. Blumgart, and Y. Fong, "Patterns of initial disease recurrence after resection of gallbladder carcinoma and hilar cholangiocarcinoma: Implications for adjuvant therapeutic strategies," Cancer **98**(8), 1689–1700 (2003).
4. F. Roviello, D. Marrelli, G. De Manzoni, P. Morgagni, A. Di Leo, L. Saragoni, and A. De Stefano, "Prospective study of peritoneal recurrence after curative surgery for gastric cancer," Br. J. Surg. **90**(9), 1113–1119 (2003).
5. T. Schnelldorfer, A. L. Ware, M. G. Sarr, T. C. Smyrk, L. Zhang, R. Qin, R. E. Gullerud, J. H. Donohue, D. M. Nagorney, and M. B. Farnell, "Long-term survival after pancreatoduodenectomy for pancreatic adenocarcinoma is cure possible?" Ann. Surg. **247**(3), 456–462 (2008).
6. A. M. Van Altena, E. Kolwijck, M. J. B. Spanjer, J. C. M. Hendriks, L. F. A. G. Massuger, and J. A. De Hullu, "CA125 nadir concentration is an independent predictor of tumor recurrence in patients with ovarian cancer: a population-based study," Gynecologic Oncol. **119**(2), 265–269 (2010).
7. V. Gallotta, S. Y. Jeong, C. Conte, R. Trozzi, S. Cappuccio, R. Moroni, G. Ferrandina, G. Scambia, T.-J. Kim, and A. Fagotti, "Minimally invasive surgical staging for early stage ovarian cancer: A long-term follow up," European J. Surg. Oncol. **47**(7), 1698–1704 (2021).
8. T. Schnelldorfer, M. P. Ware, L. P. Liu, M. G. Sarr, D. H. Birkett, and R. Ruthazer, "Can we accurately identify peritoneal metastases based on their appearance? An assessment of the current practice of intraoperative gastrointestinal cancer staging," Ann. Surg. Oncol. **26**(6), 1795–1804 (2019).
9. D. Pouli, E. M. Genega, T. B. Sullivan, K. M. Rieger-Christ, V. Wright, I. Georgakoudi, and T. Schnelldorfer, "Two-photon images reveal unique texture features for label-free identification of ovarian cancer peritoneal metastases," Biomed. Opt. Express **10**(9), 4479–4488 (2019).
10. C. Uhler and G. Shivashankar, "Nuclear mechanopathology and cancer diagnosis," Trends in Cancer **4**(4), 320–331 (2018).
11. R. Baghban, L. Roshangar, R. Jahanban-Esfahlan, K. Seidi, A. Ebrahimi-Kalan, M. Jaymand, S. Kolahian, T. Javaheri, and P. Zare, "Tumor microenvironment complexity and therapeutic implications at a glance," Cell Commun. Signal. **18**(1), 59 (2020).
12. S. Xu, H. Xu, W. Wang, S. Li, H. Li, T. Li, W. Zhang, X. Yu, and L. Liu, "The role of collagen in cancer: from bench to bedside," J. Transl. Med. **17**, 309 (2019).
13. A. Keikhosravi, J. S. Bredfeldt, A. K. Sagar, and K. W. Eliceiri, "Second-harmonic generation imaging of cancer," Methods Cell Biol. **123**, 531–546 (2014).
14. L. T. Perelman, "Optical diagnostic technology based on light scattering spectroscopy for early cancer detection," Expert Rev. Med. Devices **3**(6), 787–803 (2006).
15. J. Vizet, J. Rehbinder, S. Deby, S. Roussel, A. Nazac, R. Soufan, C. Genestie, C. Haie-Meder, H. Fernandez, and F. Moreau, "In vivo imaging of uterine cervix with a Mueller polarimetric colposcope," Sci. Rep. **7**(1), 2471 (2017).
16. A. Pierangelo, S. Manhas, A. Benali, C. Fallet, J.-L. Totobenazara, M. R. Antonelli, T. Novikova, B. Gayet, A. De Martino, and P. Validire, "Multispectral Mueller polarimetric imaging detecting residual cancer and cancer regression after neoadjuvant treatment for colorectal carcinomas," J. Biomed. Opt. **18**(4), 046014 (2013).
17. A. Pierangelo, A. Nazac, A. Benali, P. Validire, H. Cohen, T. Novikova, B. H. Ibrahim, S. Manhas, C. Fallet, and M.-R. Antonelli, "Polarimetric imaging of uterine cervix: a case study," Opt. Express **21**(12), 14120–14130 (2013).
18. J. Chung, W. Jung, M. J. Hammer-Wilson, P. Wilder-Smith, and Z. Chen, "Use of polar decomposition for the diagnosis of oral precancer," Appl. Opt. **46**(15), 3038–3045 (2007).
19. J. Ramella-Roman, I. Saytashev, and M. Piccini, "A review of polarization-based imaging technologies for clinical and pre-clinical applications," J. Opt. **22**(12), 123001 (2020).
20. J. Qi and D. S. Elson, "Mueller polarimetric imaging for surgical and diagnostic applications: a review," J. Biophotonics **10**(8), 950–982 (2017).
21. C. He, H. He, J. Chang, B. Chen, H. Ma, and M. J. Booth, "Polarisation optics for biomedical and clinical applications: A review," Light: Sci. Appl. **10**(1), 1–20 (2021).
22. Y. Dong, J. Wan, L. Si, Y. Meng, Y. Dong, S. Liu, H. He, and H. Ma, "Deriving polarimetry feature parameters to characterize microstructural features in histological sections of breast tissues," IEEE Trans. Biomed. Eng. **68**(3), 881–892 (2021).
23. R. Patel, A. Khan, D. J. Wirth, M. Kamionek, D. Kandil, R. Quinlan, and A. N. Yaroslavsky, "Multimodal optical imaging for detecting breast cancer," J. Biomed. Opt. **17**(6), 066008 (2012).
24. Y. Dong, S. Liu, Y. Shen, H. He, and H. Ma, "Probing variations of fibrous structures during the development of breast ductal carcinoma tissues via Mueller matrix imaging," Biomed. Opt. Express **11**(9), 4960–4975 (2020).
25. S. Stoff, J. Chue-Sang, N. A. Holness, A. Gandjbakhche, V. Chernomordik, and J. Ramella-Roman, "Cervical collagen imaging for determining preterm labor risks using a colposcope with full Mueller matrix capability," Proc. SPIE **9689**, 968947 (2016).
26. J. Rehbinder, H. Haddad, S. Deby, B. Teig, A. Nazac, T. Novikova, A. Pierangelo, and F. Moreau, "Ex vivo Mueller polarimetric imaging of the uterine cervix: a first statistical evaluation," J. Biomed. Opt. **21**(7), 071113 (2016).

Biomedical Optics EXPRESS

27. J. Chue-Sang, N. Holness, M. Gonzalez, J. Greaves, I. Saytashev, S. Stoff, A. Gandjbakhche, V. V. Chernomordik, G. Burkett, and J. C. Ramella-Roman, "Use of Mueller matrix colposcopy in the characterization of cervical collagen anisotropy," J. Biomed. Opt. **23**(12), 1 (2018).
28. J. Chue-Sang, Y. Bai, S. Stoff, M. Gonzalez, N. A. Holness, J. Gomes, R. Jung, A. H. Gandjbakhche, V. V. Chernomordik, and J. C. Ramella-Roman, "Use of Mueller matrix polarimetry and optical coherence tomography in the characterization of cervical collagen anisotropy," J. Biomed. Opt. **22**(8), 1–9 (2017).
29. I. Ahmad, M. Ahmad, K. Khan, S. Ashraf, S. Ahmad, and M. Ikram, "Ex vivo characterization of normal and adenocarcinoma colon samples by Mueller matrix polarimetry," J. Biomed. Opt. **20**(5), 056012 (2015).
30. T. Novikova, A. Pierangelo, S. Manhas, A. Benali, P. Validire, B. Gayet, and A. De Martino, "The origins of polarimetric image contrast between healthy and cancerous human colon tissue," Appl. Phys. Lett. **102**(24), 241103 (2013).
31. A. Pierangelo, S. Manhas, A. Benali, C. Fallet, M.-R. Antonelli, T. Novikova, B. Gayet, P. Validire, and A. De Martino, "Ex vivo photometric and polarimetric multilayer characterization of human healthy colon by multispectral Mueller imaging," J. Biomed. Opt. **17**(6), 066009 (2012).
32. A. Pierangelo, A. Benali, M. R. Antonelli, T. Novikova, P. Validire, B. Gayet, and A. De Martino, "Ex-vivo characterization of human colon cancer by Mueller polarimetric imaging," Opt. Express **19**(2), 1582–1593 (2011).
33. A. N. Yaroslavsky, J. G. Barbosa, V. Neel, C. A. DiMarzio, and R. R. Anderson, "Combining multispectral polarized light imaging and confocal microscopy for localization of nonmelanoma skin cancer," J. Biomed. Opt. **10**(1), 014011 (2005).
34. E. Du, H. He, N. Zeng, M. Sun, Y. Guo, J. Wu, S. Liu, and H. Ma, "Mueller matrix polarimetry for differentiating characteristic features of cancerous tissues," J. Biomed. Opt. **19**(7), 076013 (2014).
35. P. Ghassemi, P. Lemaillet, J. C. Ramella-Roman, J. W. Shupp, S. S. Venna, M. E. Boisvert, K. Flanagan, M. H. Jordan, and T. A. Germer, "Out-of-plane Stokes imaging polarimeter for early skin cancer diagnosis," J. Biomed. Opt. **17**(7), 0760141 (2012).
36. K. L. Sodek, K. J. Murphy, T. J. Brown, and M. J. Ringuette, "Cell-cell and cell-matrix dynamics in intraperitoneal cancer metastasis," Cancer Metastasis Rev. **31**(1-2), 397–414 (2012).
37. S. L. Jacques, K. Lee, and J. C. Ramella-Roman, "Scattering of polarized light by biological tissues," in *Saratov Fall Meeting'99: Optical Technologies in Biophysics and Medicine*, (International Society for Optics and Photonics, 2000), 14–28.
38. Y. Liu, Y. L. Kim, X. Li, and V. Backman, "Investigation of depth selectivity of polarization gating for tissue characterization," Opt. Express **13**(2), 601–611 (2005).
39. S. L. Jacques, J. R. Roman, and K. Lee, "Imaging superficial tissues with polarized light," Lasers Surg. Med. **26**(2), 119–129 (2000).
40. X. Feng, R. Patel, and A. N. Yaroslavsky, "Wavelength optimized cross-polarized wide-field imaging for noninvasive and rapid evaluation of dermal structures," J. Biophotonics **8**(4), 324–331 (2015).
41. M. Gonzalez, K. A. Montejo, K. Krupp, V. Srinivas, E. DeHoog, P. Madhivanan, and J. C. Ramella-Roman, "Design and implementation of a portable colposcope Mueller matrix polarimeter," J. Biomed. Opt. **25**(11), 116006 (2020).
42. M. Gonzalez and J. Ramella-Roman, "4×3 Mueller matrix imager for cervical health diagnosis," in *Polarized Light and Optical Angular Momentum for Biomedical Diagnostics*, (International Society for Optics and Photonics, 2021), 116460H.
43. J. C. Ramella-Roman, M. Gonzalez, J. Chue-Sang, K. Montejo, K. Krup, V. Srinivas, E. DeHoog, and P. Madhivanan, "Development and characterization of a snapshot Mueller matrix polarimeter for the determination of cervical cancer risk in the low resource setting," in *Optics and Biophotonics in Low-Resource Settings IV*, (International Society for Optics and Photonics, 2018), 104850X.
44. J. Qi, C. He, and D. S. Elson, "Real time complete Stokes polarimetric imager based on a linear polarizer array camera for tissue polarimetric imaging," Biomed. Opt. Express **8**(11), 4933–4946 (2017).
45. J. Qi and D. S. Elson, "A high definition Mueller polarimetric endoscope for tissue characterisation," Sci. Rep. **6**(1), 25953 (2016).
46. J. Qi, M. Singh, N. Clancy, and D. Elson, "Mueller polarimetric endoscopy," in *CLEO: Applications and Technology*, (Optical Society of America, 2014), AM2O. 1.
47. J. Qi, M. Ye, M. Singh, N. T. Clancy, and D. S. Elson, "Narrow band 3× 3 Mueller polarimetric endoscopy," Biomed. Opt. Express **4**(11), 2433–2449 (2013).
48. M. R. Antonelli, A. Pierangelo, T. Novikova, P. Validire, A. Benali, B. Gayet, and A. De Martino, "Mueller matrix imaging of human colon tissue for cancer diagnostics: how Monte Carlo modeling can help in the interpretation of experimental data," Opt. Express **18**(10), 10200–10208 (2010).
49. N. T. Clancy, S. Arya, J. Qi, D. Stoyanov, G. B. Hanna, and D. S. Elson, "Polarised stereo endoscope and narrowband detection for minimal access surgery," Biomed. Opt. Express **5**(12), 4108–4117 (2014).
50. A. Pigula, N. T. Clancy, S. Arya, G. B. Hanna, and D. S. Elson, "Video-rate dual polarization multispectral endoscopic imaging," Proc. SPIE **9333**, 93330N (2015).
51. T. C. Wood and D. S. Elson, "Polarization response measurement and simulation of rigid endoscopes," Biomed. Opt. Express **1**(2), 463–470 (2010).
52. A. Lindberg, C. Gennet, J. Vizet, J.-C. Vanel, and A. Pierangelo, "Mueller polarimetric imaging through a rigid endoscope," in *European Conference on Biomedical Optics*, (Optical Society of America, 2019), 11073_11014.

Biomedical Optics EXPRESS

53. L. Wang, S. L. Jacques, and L. Zheng, "MCML—Monte Carlo modeling of light transport in multi-layered tissues," Comput. Methods Programs Biomed. **47**(2), 131–146 (1995).
54. S. L. Jacques, "Optical properties of biological tissues: a review," Phys. Med. Biol. **58**(11), R37–R61 (2013).
55. D. Vader, A. Kabla, D. Weitz, and L. Mahadevan, "Strain-induced alignment in collagen gels," PLoS One **4**(6), e5902 (2009).
56. Z. Liu, D. Pouli, D. Sood, A. Sundarakrishnan, C. K. H. Mingalone, L. M. Arendt, C. Alonzo, K. P. Quinn, C. Kuperwasser, and L. Zeng, "Automated quantification of three-dimensional organization of fiber-like structures in biological tissues," Biomaterials **116**, 34–47 (2017).
57. Z. Liu, K. P. Quinn, L. Speroni, L. Arendt, C. Kuperwasser, C. Sonnenschein, A. M. Soto, and I. Georgakoudi, "Rapid three-dimensional quantification of voxel-wise collagen fiber orientation," Biomed. Opt. Express **6**(7), 2294–2310 (2015).
58. K. P. Quinn and I. Georgakoudi, "Rapid quantification of pixel-wise fiber orientation data in micrographs," J. Biomed. Opt. **18**(4), 046003 (2013).
59. Z. Liu, D. Pouli, D. Sood, L. M. Arendt, C. Kuperwasser, D. L. Kaplan, and I. Georgakoudi, "Three-dimensional quantification of fiber-like structures in biological tissues," in *Optical Molecular Probes, Imaging and Drug Delivery* (Optical Society of America, 2017), OmM3D. 5.
60. O. Nadiarnykh, R. B. LaComb, M. A. Brewer, and P. J. Campagnola, "Alterations of the extracellular matrix in ovarian cancer studied by Second Harmonic Generation imaging microscopy," BMC Cancer **10**(1), 94 (2010).
61. Z. Liu, D. Pouli, T. Schnelldorfer, and I. Georgakoudi, "Three-dimensional quantification of collagen fibers in cancer metastases within the peritoneal cavity," in *Cancer Imaging and Therapy*, (Optical Society of America, 2016), CTu4A. 6.
62. Y. Yang, T. Wang, N. C. Biswal, M. Brewer, Q. Zhu, X. Wang, and M. Sanders, "Optical scattering coefficient estimated by optical coherence tomography correlates with collagen content in ovarian tissue," J. Biomed. Opt. **16**(9), 090504 (2011).
63. B. Banerjee, N. S. Rial, T. Renkoski, L. R. Graves, S. A. Reid, C. Hu, V. L. Tsikitis, V. Nfonsom, J. Pugh, and U. Utzinger, "Enhanced visibility of colonic neoplasms using formulaic ratio imaging of native fluorescence," Laser Surg. Med. **45**(9), 573–581 (2013).
64. J. C. Ramella-Roman, S. A. Prahl, and S. L. Jacques, "Three Monte Carlo programs of polarized light transport into scattering media: part I," Opt. Express **13**(12), 4420–4438 (2005).
65. S. Prahl, "Mie scattering calculator. omlc. ogi. edu/calc/mie_calc. html," (Accessed, 2013).
66. A. J. Gomes, H. C. Wolfsen, M. B. Wallace, F. K. Cayer, and V. Backman, "Monte Carlo model of the depolarization of backscattered linearly polarized light in the sub-diffusion regime," Opt. Express **22**(5), 5325–5340 (2014).
67. D. Arifler, I. Pavlova, A. Gillenwater, and R. Richards-Kortum, "Light scattering from collagen fiber networks: micro-optical properties of normal and neoplastic stroma," Biophys. J. **92**(9), 3260–3274 (2007).
68. K. Komatsu and M. Chiba, "Synchronous recording of load–deformation behaviour and polarized light-microscopic images of the rabbit incisor periodontal ligament during tensile loading," Arch. Oral Biol. **46**(10), 929–937 (2001).
69. A. E. Woessner, J. D. McGee, J. D. Jones, and K. P. Quinn, "Characterizing differences in the collagen fiber organization of skin wounds using quantitative polarized light imaging," Wound Rep. Reg. **27**(6), 711–714 (2019).
70. G. Xi, W. Guo, D. Kang, J. Ma, F. Fu, L. Qiu, L. Zheng, J. He, N. Fang, and J. Chen, "Large-scale tumor-associated collagen signatures identify high-risk breast cancer patients," Theranostics **11**(7), 3229–3243 (2021).
71. P. P. Provenzano, K. W. Eliceiri, J. M. Campbell, D. R. Inman, J. G. White, and P. J. Keely, "Collagen reorganization at the tumor-stromal interface facilitates local invasion," BMC Med. **4**(1), 38 (2006).
72. P. P. Provenzano, D. R. Inman, K. W. Eliceiri, J. G. Knittel, L. Yan, C. T. Rueden, J. G. White, and P. J. Keely, "Collagen density promotes mammary tumor initiation and progression," BMC Med. **6**(1), 11–15 (2008).
73. X. Zhou, S. Maloufi, D. C. Louie, N. Zhang, Q. Liu, T. K. Lee, and S. Tang, "Investigating the depolarization property of skin tissue by degree of polarization uniformity contrast using polarization-sensitive optical coherence tomography," Biomed. Opt. Express **12**(8), 5073–5088 (2021).
74. V. Sankaran, J. T. Walsh Jr, and D. J. Maitland, "Comparative study of polarized light propagation in biologic tissues," J. Biomed. Opt. **7**(3), 300–306 (2002).
75. S. Rehn, A. Planat-Chrétien, M. Berger, J.-M. Dinten, C. Deumié-Raviol, and A. da Silva, "Depth probing of diffuse tissues controlled with elliptically polarized light," J. Biomed. Opt. **18**(1), 016007 (2013).
76. C. J. Whatcott, C. H. Diep, P. Jiang, A. Watanabe, J. LoBello, C. Sima, G. Hostetter, H. M. Shepard, D. D. Von Hoff, and H. Han, "Desmoplasia in primary tumors and metastatic lesions of pancreatic cancer," Clin. Cancer Res. **21**(15), 3561–3568 (2015).
77. G. Liu, X. Zhan, C. Dong, and L. Liu, "Genomics alterations of metastatic and primary tissues across 15 cancer types," Sci. Rep. **7**(1), 1–9 (2017).
78. A. N. Yaroslavsky, X. Feng, H. Y. Sherry, P. R. Jermain, T. W. Iorizzo, and V. A. Neel, "Dual-Wavelength optical polarization imaging for detecting skin cancer margins," J. Invest. Dermatol. **140**(10), 1994–2000.e1 (2020).
79. X. Feng, S. Doherty, I. Yaroslavsky, G. Altshuler, and A. N. Yaroslavsky, "Polarization enhanced wide-field imaging for evaluating dermal changes caused by non-ablative fractional laser treatment," Laser Surg. Med. **48**(2), 150–156 (2016).
80. A. N. Yaroslavsky, X. Feng, and V. A. Neel, "Optical mapping of nonmelanoma skin cancers—a pilot clinical study," Laser Surg. Med. **49**(9), 803–809 (2017).

Biomedical Optics EXPRESS

81. B. Fan, V. A. Neel, and A. N. Yaroslavsky, "Multimodal imaging for nonmelanoma skin cancer margin delineation," Laser Surg. Med. **49**(3), 319–326 (2017).
82. J. Chue-Sang, M. Gonzalez, A. Pierre, M. Laughrey, I. Saytashev, T. Novikova, and J. C. Ramella-Roman, "Optical phantoms for biomedical polarimetry: a review," J. Biomed. Opt. **24**(03), 1 (2019).
83. Y. Guo, N. Zeng, H. He, T. Yun, E. Du, R. Liao, Y. He, and H. Ma, "A study on forward scattering Mueller matrix decomposition in anisotropic medium," Opt. Express **21**(15), 18361–18370 (2013).
84. C. Zheng, L. W. Lau, and J. Cha, "Dual-display laparoscopic laser speckle contrast imaging for real-time surgical assistance," Biomed. Opt. Express **9**(12), 5962–5981 (2018).
85. J. Cha, B. Triana, A. Shademan, A. Krieger, P. C. Kim, and J. U. Kang, "Polarization-sensitive multispectral tissue characterization for optimizing intestinal anastomosis," Proc. SPIE **9036**, 90360H (2014).
86. Y. Yoon, S. H. Jeon, Y. H. Park, W. H. Jang, J. Y. Lee, and K. H. Kim, "Visualization of prostatic nerves by polarization-sensitive optical coherence tomography," Biomed. Opt. Express **7**(9), 3170–3183 (2016).
87. J. Qi, C. Barrière, T. C. Wood, and D. S. Elson, "Polarized multispectral imaging in a rigid endoscope based on elastic light scattering spectroscopy," Biomed. Opt. Express **3**(9), 2087–2099 (2012).
88. C. He, H. He, X. Li, J. Chang, Y. Wang, S. Liu, N. Zeng, Y. He, and H. Ma, "Quantitatively differentiating microstructures of tissues by frequency distributions of Mueller matrix images," J. Biomed. Opt. **20**(10), 105009 (2015).
89. P. Doradla, K. Alavi, C. S. Joseph, and R. H. Giles, "Terahertz polarization imaging for colon cancer detection," Proc. SPIE **8985**, 89850K (2014).